

Article

Thickness-Dependent Terahertz Permittivity of Epitaxially Grown PbTe Thin Films

Nicolas M. Kawahala ¹, Daniel A. Matos ¹, Paulo H. O. Rappl ², Eduardo Abramof ², Andrey Baydin ^{3,4}, Junichiro Kono ^{3,4,5,6} and Felix G. G. Hernandez ^{1,*}

¹ Instituto de Física, Universidade de São Paulo, São Paulo 05508-090, Brazil

² Group of Research and Development in Materials and Plasma, National Institute for Space Research, São José dos Campos 12201-970, Brazil

³ Department of Electrical and Computer Engineering, Rice University, Houston, TX 77005, USA

⁴ Smalley—Curl Institute, Rice University, Houston, TX 77005, USA

⁵ Department of Physics and Astronomy, Rice University, Houston, TX 77005, USA

⁶ Department of Material Science and NanoEngineering, Rice University, Houston, TX 77005, USA

* Correspondence: felixggh@if.usp.br

Abstract: The exceptional thermoelectric properties of PbTe are believed to be associated with the incipient ferroelectricity of this material, which is caused by strong electron–phonon coupling that connects phononic and electronic dynamics. Here, we have used terahertz time-domain spectroscopy measurements to generate complex permittivity spectra for a set of epitaxially grown PbTe thin films with thicknesses between 100 nm and 500 nm at temperatures from 10 K to 300 K. Using a Drude–Lorentz model, we retrieved the physical parameters of both the phononic and electronic contributions to the THz permittivity. We observed a strong decrease, or softening, of the transverse optical phonon mode frequency with decreasing temperature, determining a thickness-independent negative ferroelectric-transition critical temperature, while we found a thickness-dependent anharmonic phonon decay lifetime. The electronic contribution to the permittivity was larger in thinner films, and both the carrier density and mobility increased with decreasing temperature in all films. Finally, we detected a thickness-dependent longitudinal optical phonon mode frequency, indicating the presence of plasmon–phonon coupling.

Keywords: lead telluride (PbTe); thin films; terahertz optical phonons; carrier dynamics; terahertz time-domain spectroscopy (THz-TDS)



Citation: Kawahala, N.M.; Matos, D.A.; Rappl, P.H.O.; Abramof, E.; Baydin, A.; Kono, J.; Hernandez, F.G.G. Thickness-Dependent Terahertz Permittivity of Epitaxially Grown PbTe Thin Films. *Coatings* **2023**, *13*, 1855. <https://doi.org/10.3390/coatings13111855>

Academic Editor: Christian Moreau

Received: 29 September 2023

Revised: 19 October 2023

Accepted: 27 October 2023

Published: 28 October 2023



Copyright: © 2023 by the authors. Licensee MDPI, Basel, Switzerland. This article is an open access article distributed under the terms and conditions of the Creative Commons Attribution (CC BY) license (<https://creativecommons.org/licenses/by/4.0/>).

1. Introduction

To provide insight into the excellent thermoelectric properties of lead telluride (PbTe), much attention has been recently paid to its phononic properties [1–3]. It has long been known that PbTe, along with some other IV–VI compounds, exhibits a structural phase transition, from the rock salt to the rhombohedral structure [4], accompanied by an increasing ferroelectric instability with decreasing temperature [5], a property shared by good thermoelectric materials [6]. At finite temperatures, PbTe is in a paraelectric phase, characterized by a substantial temperature dependence of its static dielectric constant, concomitant with a softening of the transverse optical (TO) phonon mode with decreasing temperature. Giant anharmonic coupling of this TO phonon mode with heat-carrying longitudinal acoustic (LA) phonons is believed to be related to the low thermal conductivity of PbTe [7–10].

Even though a paraelectric-to-ferroelectric phase transition does not occur in PbTe at a finite temperature, being energetically close to the transition to a non-centrosymmetric structure (with a presumed negative critical temperature), makes the crystal lattice highly susceptible to external perturbations [11]. For instance, recent measurements of PbTe thin films subject to high magnetic fields indicated field-induced morphic changes in crystal symmetries, observed through the chirality of circularly polarized phonons [12].

The magnetic moment of these chiral phonons can be controlled by electron–phonon coupling [13,14], and evidence for plasmon–phonon coupling has recently been reported for the longitudinal optical (LO) phonon mode in PbTe under photogeneration of free carriers [15]. Therefore, it should be insightful to study free-carrier dynamics, in addition to phonon dynamics, as well as their interplay. Furthermore, chalcogenide materials including the alloy family of tellurium display a phase-changing phenomena that can be exploited for active terahertz (THz) photonic applications [16–21].

The relatively low frequency of the soft TO phonon mode in PbTe, slightly below 1 THz at room temperature, makes it suitable for being probed through terahertz spectroscopy techniques, as this mode is infrared (IR) active. In this work, we performed THz time-domain spectroscopy (THz-TDS) [22] measurements to simultaneously determine the real and imaginary parts of the complex permittivity (dielectric function) in PbTe thin films. By investigating samples with different film thicknesses, we showed temperature- and thickness-dependent modifications of the dielectric response. The comparison of these observations with adequate physical models allowed us to study the phononic and electronic components in the same measurement. As a result, the data displayed the softening of the TO phonon mode with a thickness-independent ferroelectric-transition critical temperature, but with a thickness-dependent anharmonic phonon decay lifetime. On the other hand, larger electronic contributions to the permittivity were found in thinner films and an increase of the carrier density and mobility was determined as the temperature of the film decreased. Finally, from the analysis of the inferred LO phonon mode frequency, we conclude that our observations suggests the presence of phonon–plasmon coupling.

2. Samples and Methods

We studied three samples of single-crystalline PbTe thin films (with thicknesses of 100 nm, 300 nm, and 500 nm), epitaxially grown on (111) barium fluoride (BaF₂) substrates. The lattice mismatch between BaF₂ and PbTe is 4% and the linear thermal expansion coefficient of both materials are very close ($2.0 \times 10^{-5} \text{ K}^{-1}$ for PbTe and $1.8 \times 10^{-5} \text{ K}^{-1}$ for BaF₂). Barium fluoride is also transparent to radiation from the ultraviolet (0.2 μm) to the infrared (10 μm) and it has good transmittance in the THz spectral range [23]. These properties make BaF₂ a suitable substrate for the epitaxial growth of PbTe and also for optical characterization at low temperatures. The epitaxy of PbTe on (111) BaF₂ is well established in the literature [24–26]. The PbTe films were grown by molecular beam epitaxy (MBE) on fresh (111)-oriented BaF₂ substrates, cleaved from 15 mm \times 15 mm crystal bars acquired from Korth Krystalle GmbH, in a RIBER 32P MBE system. The 1 mm-thick BaF₂ slices were glued to a molybdenum block using a Ga–In eutectic alloy and introduced in the MBE load-lock chamber. For this experiment we used one effusion cell charged with a metal rich source (Pb_{0.505}Te_{0.495}) and two extra tellurium cells to account for Te loss during deposition. Before and after growth, the beam equivalent pressure (BEP) of each cell was measured separately in a Bayert-Alpert ion gauge placed at the substrate position. Before growth, the substrate was degassed at 150 °C for 30 min in the preparation chamber and thermal cleaned at 500 °C for 10 min in the main chamber. For all growths, the substrate temperature was kept at 240 °C and the BEP values of PbTe and both Te effusion cells were 1.0×10^{-6} Torr and 6.0×10^{-8} Torr, respectively. These conditions lead to a growth rate of approximately 0.13 nm/s. Reflection high-energy electron diffraction (RHEED) system with an electron gun set to 16 keV was used to evaluate in situ the deposition conditions. Prior to growth, the RHEED pattern of the bare BaF₂ showed diffraction points lying on a semicircle, characteristic of a pristine flat substrate surface. As deposition begins, the RHEED pattern changes immediately to fixed spots on the screen, typical of a transmission pattern, showing that the deposition starts with the nucleation of islands. After 6 min of deposition (\sim 50 nm), the RHEED pattern slowly switches to elongated spots on a semicircle, indicating that the islands coalesce and a step-flow growth mode takes place, which remains until the end of growth. As reported in ref. [26], for a 2 μm -thick film of PbTe/BaF₂ epitaxially grown in our MBE system under the same conditions used here, the X-ray diffraction curves measured

around the (222) Bragg point exhibit only the (222) peaks of film and substrate with a full width at half maximum (FWHM) of around 100 arcsec. Thus, both RHEED and X-ray diffraction results demonstrate that single-crystalline PbTe films result from MBE growth on (111) BaF₂ substrates.

We used THz-TDS in a transmission geometry, as shown in Figure 1a. THz radiation was generated with a biased photoconductive antenna (PCA) pumped by pulses from a mode-locked Ti:sapphire laser oscillator tuned to 780 nm, with a pulse duration of 130 fs and a repetition rate of 76 MHz. The THz beam was focused onto the sample with a 3 mm spot diameter, incident onto the film-coated face. The transmitted beam leaving the back of the substrate was collected and probed by another optically gated PCA, allowing recording of the THz electric field in the time domain. Low-temperature measurements were enabled by mounting the sample inside a cold finger cryocooler equipped with polytetrafluoroethylene windows.

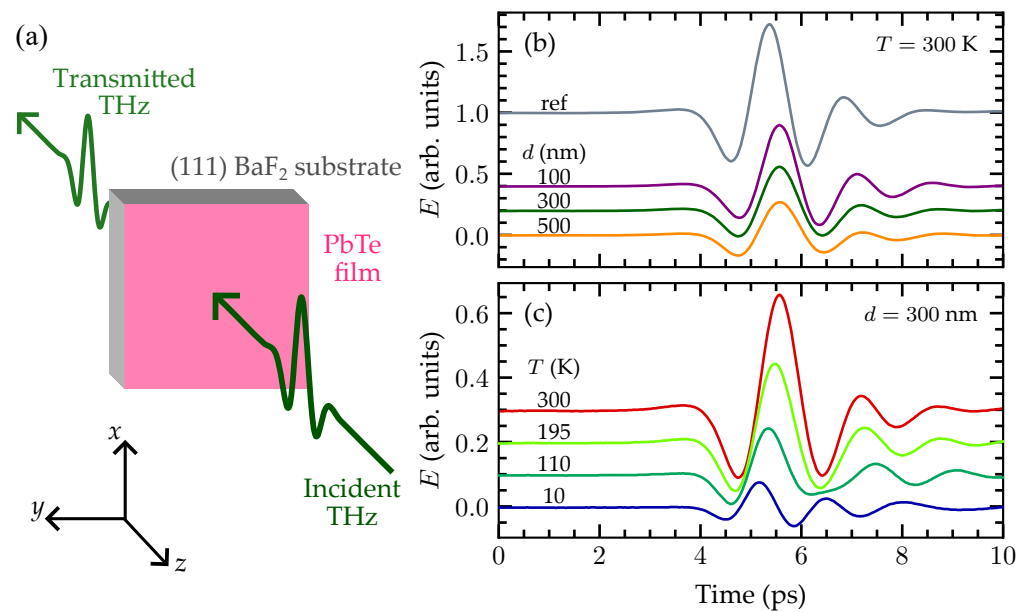


Figure 1. (a) Schematic diagram of the THz-TDS setup in transmission geometry. (b) Time-domain waveforms of the THz electric field pulses transmitted through samples with different PbTe film thicknesses d , at room temperature, in comparison with a substrate-only reference measurement (ref). (c) Temperature-induced changes in the THz pulses transmitted through the 300 nm-thick sample, for a few temperatures. The curves are vertically offset for clarity.

We retrieved time-domain data at temperatures T between 10 K to 300 K, not only for each sample with a particular film thickness d , but also for a substrate-only sample as a reference. Figure 1b shows the detected time-domain signals for all samples at room temperature ($T = 300$ K), truncated in a 10 ps time window, including a trace for the reference sample. Additionally, Figure 1c shows transmitted THz waveforms for the $d = 300$ nm sample at various T .

As a measurement with the THz-TDS technique outputs the transient electric field of a THz pulse, the gathered time-domain data were Fourier transformed for the retrieval of both the amplitude and phase components of the frequency-dependent THz electric fields, which contain the spectral response of the whole transmission system. Hence, for each sample containing a PbTe film of thickness d , at a given temperature T , the film contribution may be isolated through the determination of the complex transmission coefficient

$$\mathcal{T}_{d,T}(\nu) = \frac{E_{d,T}(\nu)}{E_{\text{ref},T}(\nu)} \exp \left[\frac{2\pi i \nu}{c} (1-n)\Delta L \right] \quad (1)$$

where $E_{d,T}(\nu)$ and $E_{ref,T}(\nu)$ are, respectively, the frequency (ν)-dependent sample and reference electric fields, c is the speed of light in vacuum, n is the BaF₂ substrate refractive index, and ΔL is the small thickness difference between sample and reference substrates.

The frequency-dependent complex permittivity $\epsilon(\nu) = \epsilon_1(\nu) + i\epsilon_2(\nu)$ of a film with thickness d at temperature T can be determined through

$$\epsilon_{d,T}(\nu) = i(1+n) \left[\frac{1}{\mathcal{T}_{d,T}(\nu)} - 1 \right] \frac{c}{2\pi\nu d} - n \quad (2)$$

where $\mathcal{T}_{d,T}(\nu)$ is the complex transmission coefficient given by Equation (1). Equation (2) can be derived using conventional transmission models in the thin film limit [27,28].

3. Results

Figure 2 shows a summary of the real (top row) and imaginary (bottom row) parts of the complex permittivity extracted from the THz-TDS measurements of the PbTe thin films using Equation (2) for several temperatures. A prominent resonance feature is observed, which becomes stronger and sharper, and shifts toward lower frequencies, as the temperature decreases from 300 K (red curves) to 10 K (blue curves). This strongly temperature-dependent resonance has been previously attributed to the soft TO phonon mode in PbTe, which is in turn associated with the ferroelectric instability in the crystal structure [5]. Further, the lineshape of this resonance is notably asymmetric, suggesting that an additional non-negligible free-carrier component must be accounted for when describing the dynamics of the system.

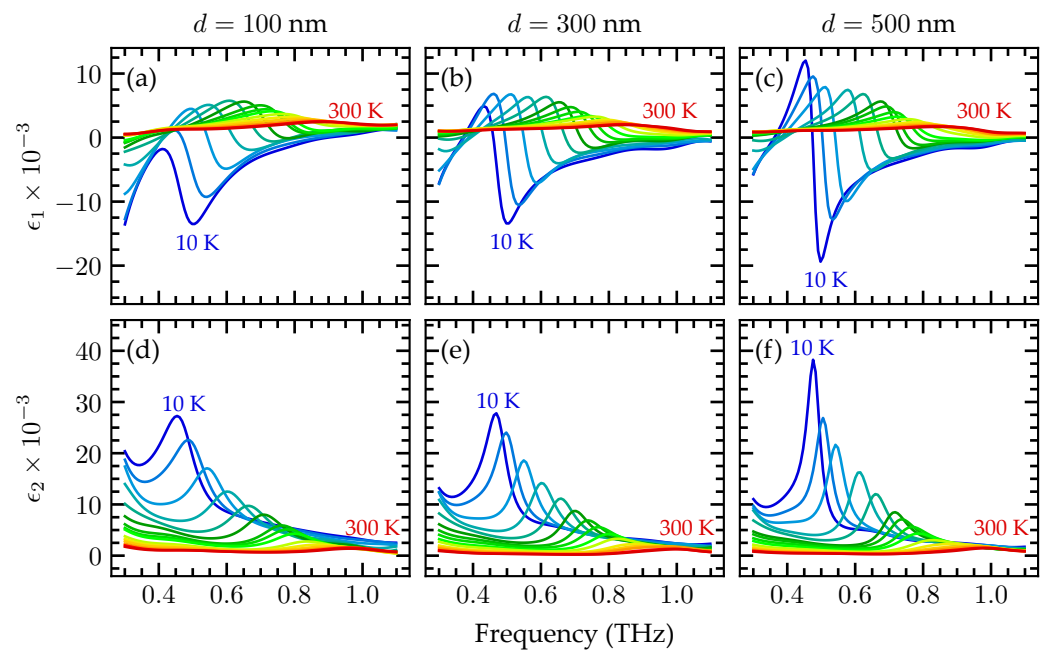


Figure 2. (a–c) Real and (d–f) imaginary parts of the frequency-dependent permittivity curves of the PbTe films, extracted from THz-TDS measurements for several temperatures (step of 20 K) between 10 K (blue curves) to 300 K (red curves). Each column in the grid of figure panels corresponds to the results for a particular film thickness considered in this study.

To separate the phononic and electronic contributions to the permittivity curves presented in Figure 2, we used a model that treats the TO phonon as a damped Lorentz

oscillator with an addition of a free-carrier permittivity correction within the Drude model. Namely, we employed the following equation to fit the experimental curves [4]:

$$\epsilon(\nu) = \epsilon_\infty + \frac{(\epsilon_s - \epsilon_\infty)\nu_{TO}^2}{\nu_{TO}^2 - \nu^2 - i\nu\Gamma_{TO}} - \frac{\nu_p^2}{\nu^2 + i\nu\gamma} \tag{3}$$

where ϵ_∞ and ϵ_s are the high-frequency and static dielectric constants, ν_{TO} and Γ_{TO} are the TO phonon central frequency and linewidth, γ is the carrier collision rate, and ν_p is the plasma frequency [29].

In the optimization process, we varied all parameters in Equation (3) to find optimal simultaneous fits to both the real and imaginary parts of the complex permittivity data. As an example, Figure 3 shows, separately for ϵ_1 and ϵ_2 , how the fitted curves (black dashed lines) compare with the experimental permittivity for the 300 nm PbTe thin film at 10 K (blue circles) and 300 K (red squares). Finally, Figure 4 presents the temperature dependence of the optimal parameters resulting from the fitting process. For all samples, data points are represented as purple circles for $d = 100$ nm, green squares for $d = 300$ nm, and orange triangles for $d = 500$ nm.

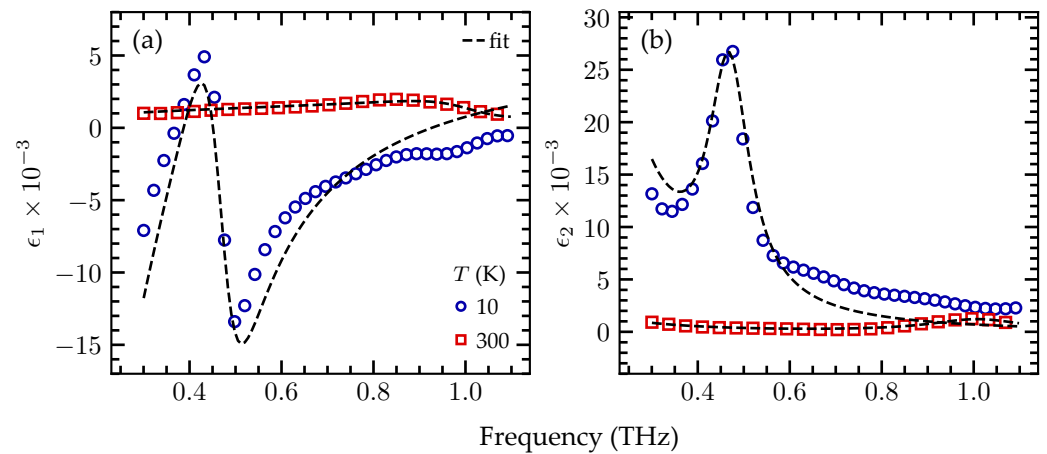


Figure 3. (a) Real and (b) imaginary parts of the permittivity data for the 300 nm PbTe thin film at 10 K (blue circles) and 300 K (red squares) with the optimal fits using Equation (3) (black dashed lines).

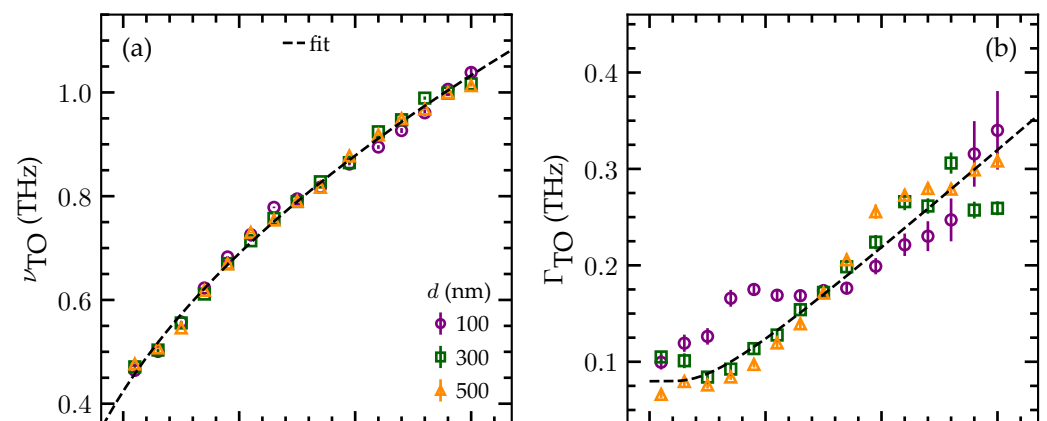


Figure 4. Cont.

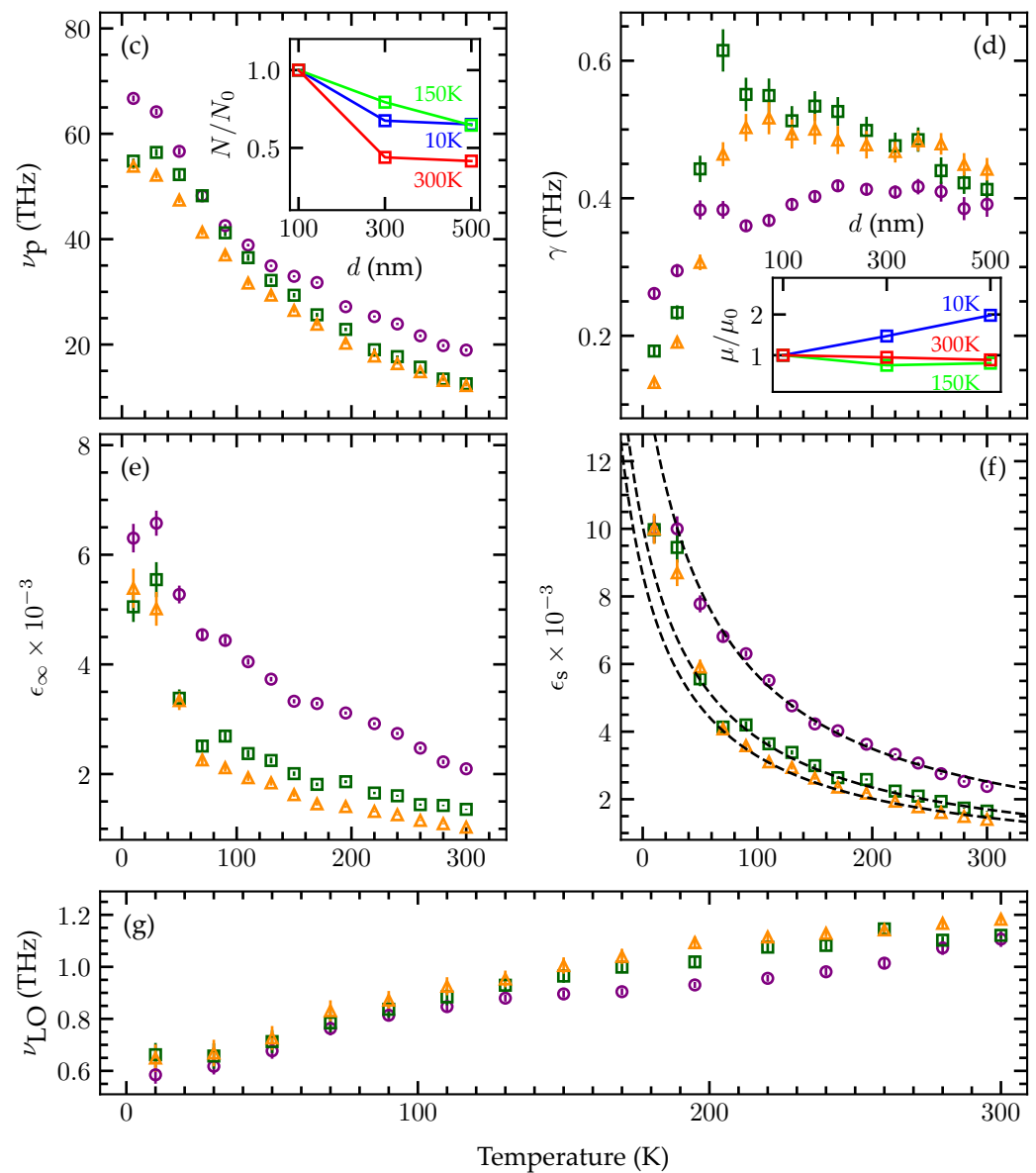


Figure 4. For all investigated film thicknesses, the optimized parameters found through the fit of the model to the permittivity data are presented as a function of the temperature. (a) TO phonon central frequency; (b) TO phonon linewidth; (c) plasma frequency (inset: carrier density variation); (d) carrier collision rate (inset: carrier mobility variation); (e) high-frequency dielectric constant; and (f) static dielectric constant. Additionally, (g) shows the LO phonon frequency as computed from the ν_{TO} , ϵ_{∞} , and ϵ_s data.

4. Discussion

Let us first consider the TO phonon central frequency ν_{TO} , as displayed in Figure 4a, where the same well-behaved temperature dependence was obtained for all samples under investigation, regardless of the film thickness. As each film was cooled down from 300 K to 10 K, a decrease in ν_{TO} from around 1.04 THz to 0.47 THz was observed, which is compatible with the frequency shift of the resonances in the permittivity curves shown in Figure 2. If we assume that the PbTe films are in a paraelectric phase for the temperature range of the experiments, the static dielectric constant should obey a Curie-Weiss law of the form [30]

$$\epsilon_s(T) \propto (T - T_c)^{-1} \tag{4}$$

which is equivalent to the expected temperature dependence of the TO phonon central frequency given by [31,32]

$$\nu_{\text{TO}}(T) \propto \sqrt{T - T_c} \quad (5)$$

where T_c is the Curie temperature for the ferroelectric phase transition. Equations (4) and (5) are connected through the Lyddane–Sachs–Teller relation (LST) [33,34]

$$\frac{\nu_{\text{LO}}^2}{\nu_{\text{TO}}^2} = \frac{\epsilon_s}{\epsilon_\infty} \quad (6)$$

thus leading to the product of the LO phonon frequency ν_{LO} with the high-frequency dielectric constant not depending on the temperature.

Simultaneous fits of Equation (5) to all data points collected for all samples, shown in Figure 4a (black dashed line), are in excellent agreement with the observations, therefore corroborating the ferroelectric instability of the crystal structure originating from the reported softening of ν_{TO} . As a result, a Curie temperature of $T_c = (-60 \pm 2)$ K was obtained for this system, independent of the film thickness.

The temperature dependence of the TO phonon linewidth Γ_{TO} shown in Figure 4b is consistent with the sharpening of the resonance with decreasing T shown in Figure 2. Additionally, because the TO phonon linewidth can be considered the inverse of its lifetime (assuming that it is homogeneously broadened), we can interpret the behavior in Figure 4b as a faster decay with increasing T , in agreement with what is expected for an anharmonic decay of an optical phonon into two acoustic phonons with finite momentum [12,35]. Overall, TO phonon lifetimes on the order of few picoseconds are shown to increase with d at $T < 150$ K, with an average increase of 50 % in its value as the film thickness is increased from 100 nm to 500 nm. Conversely, at higher T , this behavior seems to revert, displaying a lifetime that decreases with d , roughly dropping to 85 % of its value in the same film thickness increment considered above.

Concerning the free carrier contribution to the permittivity, let us first analyze the behavior of the plasma frequency

$$\nu_p = \frac{1}{2\pi} \sqrt{\frac{Ne^2}{\epsilon_0 m^*}} \quad (7)$$

where e is the electron charge, ϵ_0 is the vacuum permittivity, and m^* is the T -dependent carrier effective mass [36]. As can be seen in Figure 4c, the value of ν_p more than triples as T decreases from 300 K to 10 K, while it decreases with d . Independently of the T dependence of m^* , our results indicate that N decreases with increasing T or d . On average, N was observed to increase by over 50 % upon decreasing d from 500 nm to 100 nm, as illustrated in the inset to Figure 4c, where $N_0(T) = N(T, d = 100 \text{ nm})$ is defined as the carrier density of the 100 nm-thick film at each T . We estimate $N_0(10 \text{ K}) \approx 2.2 \times 10^{18} \text{ cm}^{-3}$ and $N_0(300 \text{ K}) \approx 0.6 \times 10^{18} \text{ cm}^{-3}$, using values for m^* from ref. [36].

Figure 4d shows the extracted carrier collision rate γ . The mean free time, on the order of a few picoseconds, decreases as T is increased from 10 K to around 100 K but saturates for $T > 100$ K. Since the carrier mobility depends on γ through

$$\mu = \frac{e}{\gamma m^*} \quad (8)$$

the mobility increases with decreasing T in the low- T range but saturates for $T > 100$ K. At the lowest temperatures, μ increases as with increasing d , which is in agreement with the literature for zero- T carrier mobility extracted from resistivity measurements [37]. The inset to Figure 4d shows the d dependence of μ/μ_0 for a few temperatures, where $\mu_0(T) \equiv \mu(T, d = 100 \text{ nm})$ is the carrier mobility for the 100 nm-thick film at each T . We estimate $\mu_0(10 \text{ K}) \approx 16 \times 10^4 \text{ cm}^2/\text{Vs}$ and $\mu_0(300 \text{ K}) \approx 3 \times 10^4 \text{ cm}^2/\text{Vs}$, using values for

m^* from ref. [36]. Considering the observed d dependence, these values for both N and μ are compatible with results of transport measurements in 1.6 μm -thick PbTe films [38].

Finally, the extracted behaviors for the high-frequency and static dielectric constants are presented in Figure 4e,f, respectively, with values on the order of 10^3 that matches the high values of permittivity shown in Figure 2, for all samples, even outside the resonances. Overall, both ϵ_∞ and ϵ_s exhibit a similar dependence on d , i.e., increasing with decreasing d throughout the T range of the experiments. As d decreases from 500 nm to 100 nm, the high-frequency dielectric constant was observed to double, while the static dielectric constant experienced an increase of 70%. Additionally, there is a clear T dependence for both parameters, which are discussed separately as follows.

Starting from the high-frequency side, ϵ_∞ is shown in Figure 4e to increase with decreasing T for all values of d , a behavior which resembles that reported previously for Ni-doped PbTe crystals [39], where the increase in ϵ_∞ was associated with the increase in N . Here, by comparing (c) and (e) in Figure 4, we can see that ϵ_∞ follows the increase in N , either with decreasing T or d . Likewise in Figure 4f, the static dielectric constant ϵ_s exhibits an increase as T goes down. In this case, its behavior is predicted by Equation (4), once the above analysis on the soft TO phonon frequency ν_{TO} corroborates the paraelectricity of the examined PbTe films. In fact, the fitting of Equation (4) to each data set in Figure 4f was made with the Curie temperature fixed to $T_c = -60$ K, as found above, and the resulting optimized curves depicted by the black dashed lines ended up describing well the observed T dependence of ϵ_s .

Since our observations for ϵ_s and ν_{TO} are in agreement with Equations (4) and (5), respectively, the LST relation (6) suggests that the carrier-induced T dependence retrieved for ϵ_∞ should influence the behavior of the LO phonon frequency. In this sense, Figure 4g presents ν_{LO} , determined from the data of each sample. As one can see, ν_{LO} also decreases as T is decreased from 300 K to 10 K, but differently from what was observed for the TO mode; i.e., ν_{LO} exhibits a d dependence with higher values for the thicker films. Those changes in ν_{LO} imply that the free-carrier plasmon mode $\nu_p / \sqrt{\epsilon_\infty}$ influences the LO mode, which might cause the appearance of LO phonon–plasmon coupled (LOPC) modes, as reported in other studies [15,39–41]. Moreover, the retrieved ν_{LO} values are much smaller than the value of (~ 3.4 THz) that can be found in the literature for PbTe [32,42]. Further investigations are needed to clarify the relation between our observations and the lower branch of the LOPC.

5. Conclusions

We conducted temperature-dependent THz-TDS measurements on PbTe thin films with different thicknesses, which enabled the determination of the frequency-dependent complex permittivity of the films. As characteristic features of phononic and free-carrier terms appeared on the retrieved permittivity curves, we used a model that consider these contributions to extract the dependence of typical parameters on both temperature and film thickness. Analyses of the extracted TO phonon central frequency and static dielectric constant agreed with the temperature behavior expected in the paraelectric phase of PbTe in a ferroelectric instability of the crystal structure, with a Curie temperature of (-60 ± 2) K that does not depend on the thickness of the film. Further, this soft phonon was shown to indicate anharmonic decays into two acoustic phonons with finite momentum, with a film thickness dependence that seems to act oppositely in different temperature ranges. Along with the softening of the TO phonon, we report an increase in the carrier density as the temperature of the film is lowered. This behavior is suggested by the temperature dependences of both the extracted plasma frequency and high-frequency dielectric constant. Also, the analysis of the extracted carrier collision rate indicates a carrier mobility that is quite stable for temperatures greater than 100 K but increases for decreasing temperature in the lower range. Contrary to the lack of a film thickness dependence in the TO phonon central frequency, not only the carrier density but also the static and high-frequency dielectric constants were shown to increase with decreasing thickness in a similar behavior. Moreover, the behavior of the LO phonon mode was also determined from the extracted

parameters, increasing in frequency either with increasing temperature or film thickness, which suggests the presence of LO phonon–plasmon coupling.

Author Contributions: Conceptualization, F.G.G.H.; methodology, N.M.K. and F.G.G.H.; resources, P.H.O.R. and E.A.; software, N.M.K.; investigation, N.M.K. and D.A.M.; data curation, N.M.K.; formal analysis, N.M.K.; validation, A.B.; writing—original draft, N.M.K.; writing—review & editing, F.G.G.H., A.B. and J.K.; visualization, N.M.K.; supervision, F.G.G.H.; project administration, F.G.G.H. and N.M.K.; funding acquisition, F.G.G.H. All authors have read and agreed to the published version of the manuscript.

Funding: This work was supported by the São Paulo Research Foundation (FAPESP), Grants No. 2018/06142-5 and 2023/04245-0, and the Brazilian National Council for Scientific and Technological Development (CNPq), Grants No. 141746/2019-0 and 409245/2022-4. N.M.K. acknowledges support from FAPESP Grant No. 2023/11158-6. P.H.O.R. acknowledges CNPq No. 307192/2021-0. J.K. acknowledges support from the Robert A. Welch Foundation (through Grant No. C-1509).

Institutional Review Board Statement: Not applicable.

Informed Consent Statement: Not applicable.

Data Availability Statement: All data that support the conclusions of this work are contained within the article. Additional data will be made available upon request.

Conflicts of Interest: The authors declare no conflict of interest.

Abbreviations

The following abbreviations are used in this manuscript:

BaF ₂	Barium Fluoride
BEP	Beam Equivalent Pressure
FWHM	Full Width at Half Maximum
IR	Infrared
LA	Longitudinal Acoustic
LO	Longitudinal Optical
LOPC	Longitudinal Optical Phonon–Plasmon Coupling
LST	Lyddane-Sachs-Teller relation
MBE	Molecular Beam Epitaxy
PbTe	Lead Telluride
PCA	Photoconductive Antenna
RHEED	Reflection High-Energy Electron Diffraction
TDS	Time-Domain Spectroscopy
THz	Terahertz
TO	Transverse Optical

References

1. Li, C.; Hellman, O.; Ma, J.; May, A.; Cao, H.; Chen, X.; Christianson, A.; Ehlers, G.; Singh, D.; Sales, B.; et al. Phonon Self-Energy and Origin of Anomalous Neutron Scattering Spectra in SnTe and PbTe Thermoelectrics. *Phys. Rev. Lett.* **2014**, *112*, 175501. [[CrossRef](#)] [[PubMed](#)]
2. Ju, S.; Shiga, T.; Feng, L.; Shiomi, J. Revisiting PbTe to identify how thermal conductivity is really limited. *Phys. Rev. B* **2018**, *97*, 184305. [[CrossRef](#)]
3. Xia, Y.; Hegde, V.I.; Pal, K.; Hua, X.; Gaines, D.; Patel, S.; He, J.; Aykol, M.; Wolverton, C. High-Throughput Study of Lattice Thermal Conductivity in Binary Rocksalt and Zinc Blende Compounds Including Higher-Order Anharmonicity. *Phys. Rev. X* **2020**, *10*, 041029. [[CrossRef](#)]
4. Burkhard, H.; Bauer, G.; Lopez-Otero, A. Submillimeter spectroscopy of TO-phonon mode softening in PbTe. *JOSA* **1977**, *67*, 943–946. [[CrossRef](#)]
5. Jiang, M.P.; Trigo, M.; Savić, I.; Fahy, S.; Murray, E.D.; Bray, C.; Clark, J.; Henighan, T.; Kozina, M.; Chollet, M.; et al. The origin of incipient ferroelectricity in lead telluride. *Nat. Commun.* **2016**, *7*, 12291. [[CrossRef](#)] [[PubMed](#)]
6. Chudzinski, P. Anharmonic coupling between electrons and TO phonons in the vicinity of a ferroelectric quantum critical point. *Phys. Rev. Res.* **2020**, *2*, 012048. [[CrossRef](#)]

7. Delaire, O.; Ma, J.; Marty, K.; May, A.F.; McGuire, M.A.; Du, M.H.; Singh, D.J.; Podlesnyak, A.; Ehlers, G.; Lumsden, M.D.; et al. Giant anharmonic phonon scattering in PbTe. *Nat. Mater.* **2011**, *10*, 614–619. [[CrossRef](#)]
8. Xia, Y. Revisiting lattice thermal transport in PbTe: The crucial role of quartic anharmonicity. *Appl. Phys. Lett.* **2018**, *113*, 073901. [[CrossRef](#)]
9. Lu, Y.; Sun, T.; Zhang, D.B. Lattice anharmonicity, phonon dispersion, and thermal conductivity of PbTe studied by the phonon quasiparticle approach. *Phys. Rev. B* **2018**, *97*, 174304. [[CrossRef](#)]
10. Ribeiro, G.A.S.; Paulatto, L.; Bianco, R.; Errea, I.; Mauri, F.; Calandra, M. Strong anharmonicity in the phonon spectra of PbTe and SnTe from first principles. *Phys. Rev. B* **2018**, *97*, 014306. [[CrossRef](#)]
11. Melnikov, A.A.; Selivanov, Y.G.; Chekalin, S.V. Anharmonic coherent dynamics of the soft phonon mode of a PbTe crystal. *arXiv* **2023**, arXiv:2309.06549. <https://doi.org/10.48550/arXiv.2309.06549>.
12. Baydin, A.; Hernandez, F.G.G.; Rodriguez-Vega, M.; Okazaki, A.K.; Tay, F.; Noe, G.T.; Katayama, I.; Takeda, J.; Nojiri, H.; Rapp, P.H.O.; et al. Magnetic Control of Soft Chiral Phonons in PbTe. *Phys. Rev. Lett.* **2022**, *128*, 075901. [[CrossRef](#)] [[PubMed](#)]
13. Cheng, B.; Schumann, T.; Wang, Y.; Zhang, X.; Barbalas, D.; Stemmer, S.; Armitage, N.P. A Large Effective Phonon Magnetic Moment in a Dirac Semimetal. *Nano Lett.* **2020**, *20*, 5991–5996. [[CrossRef](#)] [[PubMed](#)]
14. Hernandez, F.G.G.; Baydin, A.; Chaudhary, S.; Tay, F.; Katayama, I.; Takeda, J.; Nojiri, H.; Okazaki, A.K.; Rapp, P.H.O.; Abramof, E.; et al. Chiral Phonons with Giant Magnetic Moments in a Topological Crystalline Insulator. *arXiv* **2023**, arXiv:2208.12235. <https://doi.org/10.48550/arXiv.2208.12235>.
15. Jiang, M.P.; Fahy, S.; Hauber, A.; Murray, E.D.; Savić, I.; Bray, C.; Clark, J.N.; Henighan, T.; Kozina, M.; Lindenberg, A.M.; et al. Observation of photo-induced plasmon–phonon coupling in PbTe via ultrafast X-ray scattering. *Struct. Dyn.* **2022**, *9*, 024301. [[CrossRef](#)] [[PubMed](#)]
16. Mane, R.S.; Lokhande, C.D. Chemical deposition method for metal chalcogenide thin films. *Mater. Chem. Phys.* **2000**, *65*, 1–31. [[CrossRef](#)]
17. Wuttig, M.; Yamada, N. Phase-change materials for rewriteable data storage. *Nat. Mater.* **2007**, *6*, 824–832. [[CrossRef](#)]
18. Schneider, M.N.; Rosenthal, T.; Stiewe, C.; Oeckler, O. From phase-change materials to thermoelectrics? *Z. Für Krist. Cryst. Mater.* **2010**, *225*, 463–470. [[CrossRef](#)]
19. Mochalov, L.; Kudryashov, M.; Logunov, A.; Zelentsov, S.; Nezhdanov, A.; Mashin, A.; Gogova, D.; Chidichimo, G.; De Filipo, G. Structural and optical properties of arsenic sulfide films synthesized by a novel PECVD-based approach. *Superlattices Microstruct.* **2017**, *111*, 1104–1112. [[CrossRef](#)]
20. Mochalov, L.; Dorosz, D.; Nezhdanov, A.; Kudryashov, M.; Zelentsov, S.; Usanov, D.; Logunov, A.; Mashin, A.; Gogova, D. Investigation of the composition-structure-property relationship of As_xTe_{100-x} films prepared by plasma deposition. *Spectrochim. Acta Part A Mol. Biomol. Spectrosc.* **2018**, *191*, 211–216. [[CrossRef](#)]
21. Chen, C.; Chen, S.; Lobo, R.P.; Maciel-Escudero, C.; Lewin, M.; Taubner, T.; Xiong, W.; Xu, M.; Zhang, X.; Miao, X.; et al. Terahertz Nanoimaging and Nanospectroscopy of Chalcogenide Phase-Change Materials. *ACS Photonics* **2020**, *7*, 3499–3506. [[CrossRef](#)]
22. Koch, M.; Mittleman, D.M.; Ornik, J.; Castro-Camus, E. Terahertz time-domain spectroscopy. *Nat. Rev. Methods Prim.* **2023**, *3*, 1–14. [[CrossRef](#)]
23. Kaplunov, I.A.; Kropotov, G.I.; Rogalin, V.E.; Shakhmin, A.A. Optical properties of some crystalline fluorides in the terahertz region of the spectrum. *Opt. Mater.* **2021**, *115*, 111019. [[CrossRef](#)]
24. Lopez-Otero, A. Growth of PbTe films under near-equilibrium conditions. *J. Appl. Phys.* **1977**, *48*, 446–448. [[CrossRef](#)]
25. Springholz, G.; Bauer, G.; Ihninger, G. MBE of high mobility PbTe films and PbTe/Pb_{1-x}Eu_xTe heterostructures. *J. Cryst. Growth* **1993**, *127*, 302–307. [[CrossRef](#)]
26. Rapp, P.H.O.; Closs, H.; Ferreira, S.O.; Abramof, E.; Boschetti, C.; Motisuke, P.; Ueta, A.Y.; Bandeira, I.N. Molecular beam epitaxial growth of high quality Pb_{1-x}Sn_xTe layers with $0 \leq x \leq 1$. *J. Cryst. Growth* **1998**, *191*, 466–471. [[CrossRef](#)]
27. Lloyd-Hughes, J.; Jeon, T.I. A Review of the Terahertz Conductivity of Bulk and Nano-Materials. *J. Infrared Millim. Terahertz Waves* **2012**, *33*, 871–925. [[CrossRef](#)]
28. Neu, J.; Schmuttenmaer, C.A. Tutorial: An introduction to terahertz time domain spectroscopy (THz-TDS). *J. Appl. Phys.* **2018**, *124*, 231101. [[CrossRef](#)]
29. Fox, M. *Optical Properties of Solids*, 2nd ed.; Oxford master series in condensed matter physics; Oxford University Press: New York, NY, USA, 2010.
30. Devonshire, A. Theory of ferroelectrics. *Adv. Phys.* **1954**, *3*, 85–130. [[CrossRef](#)]
31. Cochran, W. Crystal Stability and the Theory of Ferroelectricity. *Phys. Rev. Lett.* **1959**, *3*, 412–414. [[CrossRef](#)]
32. Alperin, H.A.; Pickart, S.J.; Rhyne, J.J.; Minkiewicz, V.J. Softening of the transverse-optic mode in PbTe. *Phys. Lett. A* **1972**, *40*, 295–296. [[CrossRef](#)]
33. Sievers, A.J.; Page, J.B. A generalized Lyddane-Sachs-Teller relation for solids and liquids. *Infrared Phys.* **1991**, *32*, 425–433. [[CrossRef](#)]
34. Kittel, C. *Introduction to Solid State Physics*, 8th ed.; Wiley: Hoboken, NJ, USA, 2005.
35. Klemens, P.G. Anharmonic Decay of Optical Phonons. *Phys. Rev.* **1966**, *148*, 845–848. [[CrossRef](#)]
36. Lyden, H.A. Temperature Dependence of the Effective Masses in PbTe. *Phys. Rev.* **1964**, *135*, A514–A521. [[CrossRef](#)]
37. Abd El-Ati, M.I. Electrical conductivity of PbTe thin films. *Phys. Solid State* **1997**, *39*, 68–71. [[CrossRef](#)]

38. Okazaki, A.K. Investigation of the Magnetotransport Properties in the Crystalline Topological Insulator Lead Tin Telluride. Ph.D. Thesis, INPE, São José dos Campos, Brazil, 2019.
39. Luković, D.; König, W.; Blagojević, V.; Jakšić, O.; Nikolić, P.M. Far infrared spectroscopy of PbTe doped with Ni. *Mater. Res. Bull.* **2006**, *41*, 367–375. [[CrossRef](#)]
40. Takaoka, S.; Hamaguchi, T.; Shimomura, S.; Murase, K. Observation of the coupled plasmon-LO phonon mode energy in photo-excited $\text{Pb}_{1-x}\text{Sn}_x\text{Te}$ doped with indium impurities. *Solid State Commun.* **1985**, *54*, 99–102. [[CrossRef](#)]
41. Trajic, J.; Paunovic, N.; Romcevic, M.; Slynko, V.E.; Ristic-Djurovic, J.L.; Dobrowolski, W.D.; Romcevic, N. Far infrared spectra of Si doped PbTe single crystals. *Opt. Mater.* **2019**, *91*, 195–198. [[CrossRef](#)]
42. Cochran, W.; Cowley, R.A.; Dolling, G.; Elcombe, M.M. The Crystal Dynamics of Lead Telluride. *Proc. R. Soc. Lond. Ser. A Math. Phys. Sci.* **1966**, *293*, 433–451.

Disclaimer/Publisher’s Note: The statements, opinions and data contained in all publications are solely those of the individual author(s) and contributor(s) and not of MDPI and/or the editor(s). MDPI and/or the editor(s) disclaim responsibility for any injury to people or property resulting from any ideas, methods, instructions or products referred to in the content.